

THE THREE-MM ULTIMATE MOPRA MILKY WAY SURVEY. II. CLOUD AND STAR FORMATION NEAR THE FILAMENTARY MINISTARBURST RCW 106

HANS NGUYỄN^{1,2}, QUANG NGUYỄN LƯƠNG^{1,3,4}, PETER G. MARTIN¹, PETER J. BARNES^{5, 6}, ERIK MULLER⁴, VICKI LOWE^{7,8}, NADIA LO⁹, MARIA CUNNINGHAM⁸, FRÉDÉRIQUE MOTTE¹⁰, BALTHASAR INDERMÜHLE⁷, STEFAN N. O'DOUGHERTY¹¹, AUDRA K. HERNANDEZ¹², GARY A. FULLER¹³

(Dated: Received 2014 July 10; accepted 2015 February 9; published 2015 MM DD)
Draft version August 14, 2018

ABSTRACT

We report here a study of gas, dust and star formation rates (SFRs) in the molecular cloud complexes (MCCs) surrounding the giant H II region RCW 106 using ¹²CO and ¹³CO (1-0) data from the Three-mm Ultimate Mopra Milky Way Survey (ThrUMMS) and archival data. We separate the emission in the Galactic Plane around $l = 330^\circ$ - 335° and $b = -1^\circ$ - 1° into two main MCCs: the RCW 106 ($V_{\text{LSR}} = -48 \text{ km s}^{-1}$) complex and the MCC331-90 ($V_{\text{LSR}} = -90 \text{ km s}^{-1}$) complex. While RCW 106 ($M \sim 5.9 \times 10^6 M_\odot$) is located in the Scutum-Centaurus arm at a distance of 3.6 kpc, MCC331-90 ($M \sim 2.8 \times 10^6 M_\odot$) is in the Norma arm at a distance of 5 kpc. Their molecular gas mass surface densities are ~ 220 and $\sim 130 M_\odot \text{ pc}^{-2}$, respectively. For RCW 106 complex, using the 21 cm continuum fluxes and dense clump counting, we obtain an immediate past ($\sim 0.2 \text{ Myr}$) and an immediate future ($\sim +0.2 \text{ Myr}$) SFRs of $0.25^{+0.09}_{-0.023} M_\odot \text{ yr}^{-1}$ and $0.12 \pm 0.1 M_\odot \text{ yr}^{-1}$. This results in an immediate past SFR density of $9.5^{+3.4}_{-0.9} M_\odot \text{ yr}^{-1} \text{ kpc}^{-2}$ and an immediate future SFR density of $4.8^{+3.8}_{-3.8} M_\odot \text{ yr}^{-1} \text{ kpc}^{-2}$. As both SFRs in this cloud are higher than the ministarburst threshold, they must be undergoing a ministarburst event although burst peak has already passed. We conclude that this is one of the most active star forming complexes in the southern sky, ideal for further investigations of massive star formation and potentially shedding light on the physics of high-redshift starbursts.

Subject headings: stars: formation, stars: protostars, ISM: clouds, ISM: structure, ISM: H II regions

1. INTRODUCTION

Studying the earliest phases of star formation involves examining the morphological and kinematic structure of molecular clouds and the transformation between different states of materials. Massive star formation often occurs in molecular cloud complexes (MCCs) with radius $\sim 70 \text{ pc}$ or more (e.g., W43; e.g., Nguyen Luong et al. 2011a; Motte et al. 2014), Cygnus X with radius $\sim 80 \text{ pc}$

(e.g., Schneider et al. 2006; Motte et al. 2007), and the Central Molecular Zone (CMZ) with radius $\sim 180 \text{ pc}$ (e.g., Miyazaki & Tsuboi 2000; Jones et al. 2012). MCCs associated with massive star formation reside mainly along the mid-plane of the Galaxy, may be distant and heavily obscured in the visible regime. Though not being obscured in the radio wavelength, Large-field radio surveys of MCCs generally yield data sets with a substantial field of view but insufficient resolution to conduct case-by-case studies of particular clouds. This is particularly true for low resolution surveys such as the carbon monoxide (CO) survey of the Milky Way (Bronfman et al. 1989; Dame et al. 2001). While they catalog molecular clouds, the structure and properties of each cloud cannot be fully resolved. However, recent high-angular-resolution spectroscopic surveys of the Galactic plane such as the Galactic Ring Survey (GRS; Jackson et al. 2006) and the Three-mm Ultimate Mopra Milky Way Survey (ThrUMMS; Barnes et al. 2013) help to address this problem.

Of particular interest here is the MCC of gas surrounding the bright giant H II region RCW 106, which was discovered in the H α emission line survey of the southern Milky Way (Rodgers et al. 1960). The giant H II region RCW 106 hosts a cluster with mass $\sim 10^3 M_\odot$ and a Lyman continuum photon emission of 10^{50} s^{-1} , likely originating from dozens of O-type stars ($M > 8 M_\odot$). It resides in the Scutum-Centaurus arm at a distance of $\sim 3.6 \text{ kpc}$ from the Sun (Russeil et al. 2005). This makes it an excellent laboratory for testing molecular cloud formation mechanisms in response to galactic dynamical processes such as spiral density waves.

¹ Canadian Institute for Theoretical Astrophysics, University of Toronto, 60 St. George Street, Toronto, ON M5S 3H8, Canada

² Max-Planck-Institut für Radioastronomie, Auf dem Hügel 69, 53121 Bonn, Germany

³ EACOA Fellow at NAOJ, Japan & KASI, Korea

⁴ National Astronomical Observatory of Japan, Chile Observatory, 2-21-1 Osawa, Mitaka, Tokyo 181-8588, Japan

⁵ Astronomy Department, University of Florida, P.O. Box 112055, Gainesville, FL 32611, USA

⁶ School of Science and Technology, University of New England, NSW 2351, Australia

⁷ CSIRO Astronomy and Space Science, P.O. Box 76, Epping, NSW 1710, Australia

⁸ School of Physics, University of New West Wales, NSW 2052 Australia

⁹ Departamento de Astronomía, Universidad de Chile, Camino El Observatorio 1515, Las Condes, Santiago, Casilla 36-D, Chile

¹⁰ Laboratoire AIM Paris-Saclay, CEA/IRFU - CNRS/INSU - Université Paris Diderot, Service d'Astrophysique, Bât. 709, CEA-Saclay, F-91191, Gif-sur-Yvette Cedex, France

¹¹ College of Optical Sciences, University of Arizona, 1630 E. University Blvd., P.O. Box 210094, Tucson, AZ 85721, USA

¹² Astronomy Department, University of Wisconsin, 475 East Charter St., Madison, WI 53706, USA

¹³ Jodrell Bank Centre for Astrophysics, Alan Turing Building, School of Physics and Astronomy, University of Manchester, Manchester, M13 3PL, UK

† hnguyen@cita.utoronto.ca

Table 1
Observation parameters of the data used in this study

Instrument or Survey	Tracer	Frequency (GHz)	Ang. Res ($''$)	Velocity (km s^{-1})	Δv_{res} (km s^{-1})	1σ rms
CfA	^{12}CO	115.27	510	-165 to 165	1.3	0.1 K km s^{-1}
ThrUMMS	^{12}CO	115.27	72	-140 to 10	0.33	~ 3 K km s^{-1}
ThrUMMS	^{13}CO	110.20	72	-140 to 10	0.34	~ 1 K km s^{-1}
SGPS	H I	1.420	132	-	-	1.6 K km s^{-1}
SGPS	21 cm cont.	1.420	132	-	-	1 mJy beam^{-1}
MIPS/ <i>Spitzer</i>	$24\ \mu\text{m}$		6	-	-	0.01 MJy sr^{-1}
PACS/ <i>Herschel</i>	$160\ \mu\text{m}$		12	-	-	0.08 MJy sr^{-1}
SPIRE/ <i>Herschel</i>	$500\ \mu\text{m}$		37	-	-	1.2 MJy sr^{-1}

Moreover, the parent RCW 106 MCC is also the site of ongoing star formation. It is centered on $l \sim 333^\circ$, $b \sim -0^\circ.5$ and has a local standard of rest velocity $V_{\text{LSR}} \sim -50 \text{ km s}^{-1}$ (Bains et al. 2006). Its substructures have been subject to a variety of spectral line and continuum studies, progressively unravelling the star formation and evolutionary history of the region. Specifically, (Lynga 1964) and (Urquhart et al. 2007) measured the impact of UV emitted by various nearby OB stars that ionize the surrounding environment. 1.2 mm continuum maps revealed 95 clumps with masses ranging from 40 to $10^4 M_\odot$, some of which have infrared (IR) counterparts suggesting embedded star formation (Mookerjea et al. 2004). Higher density tracer such as ^{13}CO , CS, HCO^+ , HCN, and HNC emission lines show prominent velocity features centered on the V_{LSR} of RCW 106 that coincide with 1.2 mm dust clumps and are also sites of massive star formation (Bains et al. 2006; Wong et al. 2008; Lo et al. 2009). A recent NH_3 survey toward dense clumps of the RCW 106 complex revealed a large sample of cold collapsing clumps that are potentially forming stars (Lowe et al. 2014).

The two densest and most massive sites of ongoing star formation core are MMS5 and MMS68 (Mookerjea et al. 2004). They are associated with the ultracompact H II (UCHII) regions G333.6-0.2 (Fujiyoshi et al. 2005, 2006) and IRAS 16164-5096, respectively. High resolution adaptive optics observations with $0.''3$ resolution (~ 1000 AU) combined with mid-IR spectroscopy indicate the presence of mid to late-type O stars that might still be gaining mass (Grave et al. 2014).

Previous studies focused mainly on the properties of gas and dust at cloud scales of 0.1–10 pc (Mookerjea et al. 2004; Bains et al. 2006; Wong et al. 2008; Lo et al. 2009), dense clump scales of 0.1–1 pc (Lo et al. 2007, 2011), or embedded O stars subparsec scales of even smaller structure (Kumar 2013; Grave et al. 2014). In this paper we focus on the scale of the cloud complex ($\sim 50 - 100$ pc), which is the largest scale of molecular cloud in the Galaxy but the smallest scale that can be probed in nearby galaxies. On this scale, RCW 106 is a massive filamentary molecular cloud complex with an aspect ratio larger than 2: see Figure 5. Our goal is to study the global properties of the molecular clouds surrounding RCW 106 and establish a relationship between the large scale structure of these clouds and their enhanced star formation.

The various data sets used in this paper are described in Section 2. We present the two star-forming MCCs

identified using mainly the ^{12}CO emission in Section 3. The distances of these two cloud complexes are investigated in Section 4. Physical properties highlighting mass and mass surface density are discussed in Section 5. The dynamical nature of the clouds are investigated in Section 6. In Section 7, we discuss the method of predicting the SFRs and the evidence that the RCW 106 complex can be quantified as a ministarburst.

Finally, we summarize our findings in Section 8.

2. DATA

To investigate the properties of the region we used various continuum and spectral line tracers, summarized in Table 1 and discussed below.

2.1. ^{12}CO molecular line from the ThrUMMS survey

The ThrUMMS survey (Barnes et al. 2013) covers the Galactic plane between $300^\circ \leq l \leq 360^\circ$ and $-1^\circ \leq b \leq 1^\circ$ in the ^{12}CO (1–0), ^{13}CO (1–0), C^{18}O (1–0), and CN spectral lines at frequencies of 115.27, 110.20, 109.78, and 113.60 GHz, respectively.^{xv} The survey was conducted using the new Very Fast Mapping (VFM) technique developed for use with the 22 m Mopra telescope.^{xvi} Half-Nyquist sampling rates were obtained along the scanning direction and between scan rows, yielding a $72''$ resolution. Compared to the traditional on-the-fly mapping technique, the VFM technique is capable of observing a larger area in the same amount of time if Nyquist-sampled maps are not needed. As well as being more efficient, it provides a nearly uniform sensitivity per unit area. The data were converted from antenna temperature T_{ant} to main-beam temperature, T_{mb} , by dividing T_{ant} by the main-beam efficiencies η_{mb} of 0.42 for ^{12}CO (1–0), and of 0.43 for both ^{13}CO (1–0) and C^{18}O (1–0).

2.2. 21 cm continuum and H I line emission from the SGPS survey

From the Southern Galactic Plane Survey (SGPS; McClure-Griffiths et al. 2005) we extracted the H I atomic line and 21 cm continuum data over the range of $330^\circ \leq l \leq 335^\circ$ and $b = \pm 1^\circ$. The survey was conducted using the Australia Telescope Compact Array (ATCA)

^{xv} The data available to date for this study covered the range $-0^\circ.5 \leq b \leq 0^\circ.5$.

^{xvi} Operation of the Mopra radio telescope is made possible by funding from the National Astronomical Observatory of Japan, the University of New South Wales, the University of Adelaide, and the Commonwealth of Australia through CSIRO.

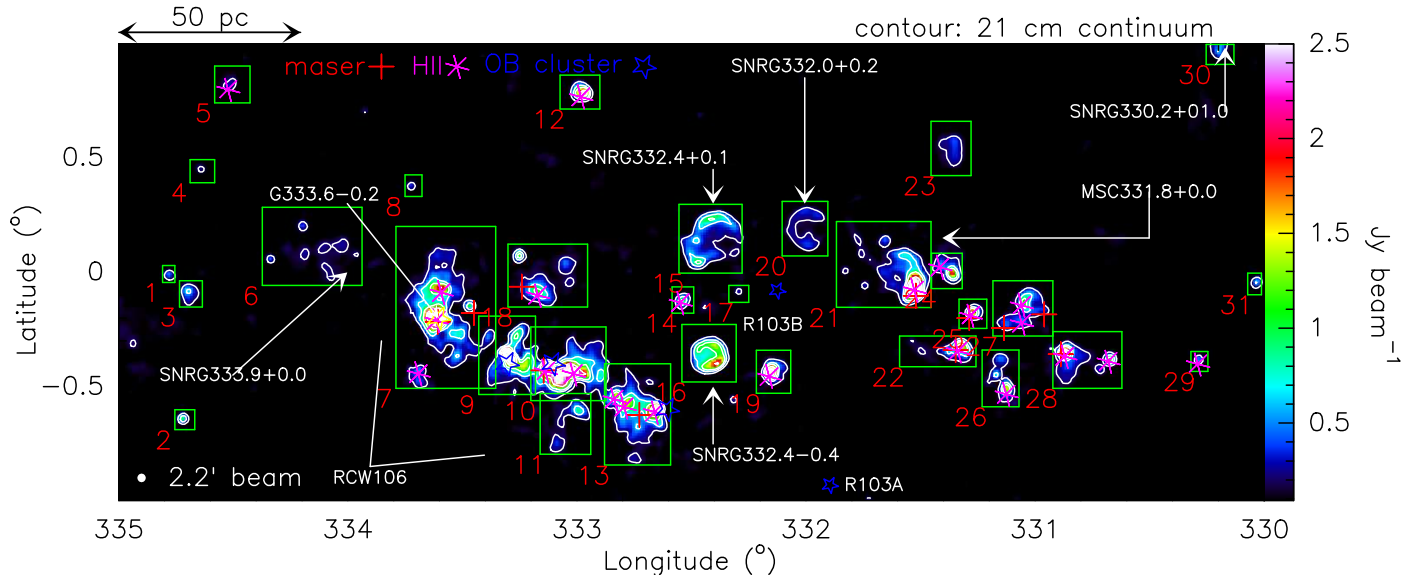


Figure 1. 21 cm continuum image (color scale) from the SGPS. Contour levels (white) are 0.2, 0.6, 1, and 2 Jy beam^{-1} . Within this region, we analysed continuum and molecular line data listed in Table 1 in 31 distinct boxes (green). The linear ruler (top of diagram) assumes a distance of 3.6 kpc. OH masers (Caswell et al. 1980) are plotted as red crosses, H II regions (Jones & Dickey 2012) as magenta asterisks, and prominent OB clusters as blue stars. Further details are given in Appendix A and Table 3.

interferometer and was complemented with the Parkes 64 m telescope ($\text{FWHM} = 15'$) for short spacings. The observations were performed simultaneously in a spectral line mode with 1024 channels across a 4 MHz bandwidth centered at 1420 MHz and in a continuum mode with 32 channels across a 128 MHz bandwidth centered at 1384 MHz (McClure-Griffiths et al. 2001, 2005). For our study, we used data which have a $\text{FWHM } 2.2'$, line rms 1.6 K km s^{-1} , and continuum rms $< 1 \text{ mJy beam}^{-1}$ (see Table 1).

2.3. Infrared data from *Herschel* and *Spitzer*

We used 160 and $250 \mu\text{m}$ images from the *Herschel Space Observatory* to examine more deeply the properties of the cold dust near RCW 106. The fields were observed as part of the *Herschel* Infrared Galactic Plane Survey (Hi-GAL; Molinari et al. 2010) at $70/160 \mu\text{m}$ with the Photodetector Array Camera and Spectrometer (PACS; Poglitsch et al. 2010) and at $250/350/500 \mu\text{m}$ with the Spectral and Photometric Imaging REceiver (SPIRE; Griffin et al. 2010). The Hi-GAL data were taken in parallel mode with a fast scanning speed of $60'' \text{ s}^{-1}$. The raw (level-0) data of each individual scan from both PACS and SPIRE were calibrated and de-glitched using HIPE^{xvii} version 11.0. The SPIRE and PACS level-1 data were then fed to version 18 of the SCANMORPHOS software package^{xviii} (Roussel 2013) to regrid and create the final maps. For our region, three Hi-Gal fields of 2.5×2.5 were combined. The resultant 160 and $500 \mu\text{m}$ images have angular resolutions of $12''$ and $37''$, and 1σ rms of 0.08 and 1.0 MJy sr^{-1} .

To trace the warm dust emission associated with high-mass star formation, we used the $24 \mu\text{m}$ image from the Multi-band Imaging Photometer for *Spitzer* Galactic

Plane Survey (*MIPSGAL*; Carey et al. 2009).

3. SPATIAL AND KINEMATIC STRUCTURE

3.1. 21 cm continuum: defining the major structures

In the 21 cm continuum image (Fig. 1) the giant H II region RCW 106 (Rodgers et al. 1960) is the largest ($1.2 \times 1^\circ$) and brightest ($\sim 287 \text{ Jy}$) area. RCW 106 is an elongated structure in $332.6 < l < 333.8$ and $-0.8 < b < 0.1$, and angled roughly 60° with respect to Galactic aast within the l, b plane (hereafter referred to as the “eastern” part). In the region $330.5 < l < 331.7$ and $-0.2 < b < 0.3$ there is another similarly angled loose structure containing bright 21 cm continuum sources (hereafter the “western” part). Between these two complexes of thermal sources there is a gap around $l \sim 332^\circ$. Projected in this gap is an OB association R103B ($332.08, -0.08$) (Mel’Nik & Efremov 1995) and also another further to the south, R103A ($331.89, -0.93$). These are at spectroscopic distances of 3.22 and 3.00 kpc, respectively, and so in the foreground. The eastern part is located at a distance of ~ 3.6 kpc and the western part is located at a distance of ~ 5 kpc.

We have further divided the map in Fig. 1 into 31 sub-regions based on a contour corresponding to the 3σ noise level above the local background. Most of the sources are H II regions whose properties are classified according to their morphologies in Appendix A. Additionally, there are four confirmed and two candidate supernova remnants (SNRs) (Green 2009). For full details of each sub-region refer to Appendix A and the summary provided in Table 3.

In Fig. 1 we also mark the positions of OH masers and H II regions found in large scale surveys (Caswell et al. 1980; Jones & Dickey 2012). The positions of masers and H II regions detected from radio recombination lines coincide with the bright radio continuum sources help to distinguish substructures and to quantify the cloud properties (see Sect. 4).

^{xvii} HIPE is a joint development software by the *Herschel* Science Ground Segment Consortium, consisting of ESA, the NASA *Herschel* Science Centre, and the HIFI, PACS, and SPIRE consortia.

^{xviii} <http://www2.iap.fr/users/roussel/herschel>

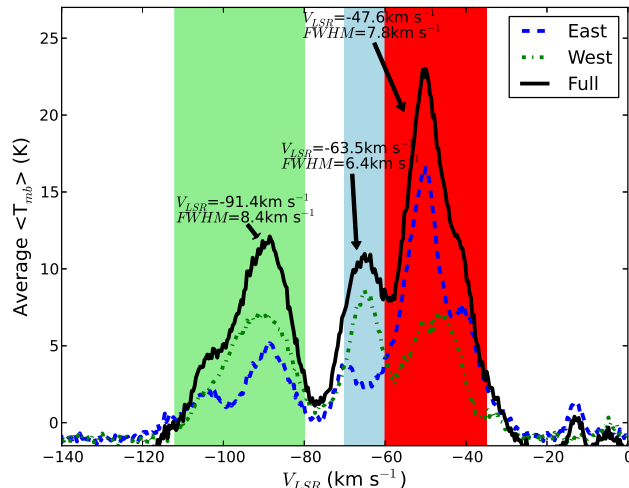


Figure 2. The ^{12}CO spectrum averaged over the entire region ($l = 330^\circ - 335^\circ$, solid black), eastern part ($l = 332^\circ.5 - 334^\circ$, dotted green), and western part ($l = 330^\circ.5 - 332^\circ.5$, dashed blue) as defined in Fig. 1.

3.2. CO and H I line emission

To investigate the relative contributions of different clouds superimposed along the line of sight, we first plot the average ^{12}CO spectrum of the entire region along with the distinctive spectra of the two main structures, eastern and western, defined in Section 3.1 (Fig. 2). In the average spectrum there are three distinct peaks within the velocity range -140 to 10 km s^{-1} . The spectra for both main structures exhibit significant peaks at roughly the same velocities, in the ranges $[-112, -80]$, $[-72, -60]$, and $[-60, -35] \text{ km s}^{-1}$ centered on $V_{LSR} = -91, -63,$ and -48 km s^{-1} , respectively. These ranges are highlighted as green, blue, and red sectors in Fig. 2. For the western region, the three spectral maxima are roughly the same, on average $\sim 7 \text{ K}$. For the eastern region, there are two peaks in the lowest velocity range, the brighter one at $V_{LSR} \sim -55 \text{ km s}^{-1}$ and the other at $\sim -45 \text{ km s}^{-1}$ (see Fig. 2). The peak at $\sim -55 \text{ km s}^{-1}$ coincides with the ^{13}CO peak that Bains et al. (2006) attributed to the cloud surrounding the RCW 106 cluster.

In Figs. 3a-c and d-f we display maps of the ^{12}CO and H I emission integrated over three velocity ranges: $[-112, -80]$, $[-80, -60]$, and $[-60, -40] \text{ km s}^{-1}$. Additionally in Fig. 3, the positions of OH masers and H II regions mostly coincide both spatially and spectrally with the molecular gas peaks.

Fig. 3a (corresponding to the green velocity range in Fig. 2) shows extended CO emission spanning the entire longitude range. Its main peak is between 331° and 332° in longitude and extends just 0.2° below the mid-plane; it covers the western region and might extend to $l = 333^\circ.4$.

The CO map integrated from -80 to -60 km s^{-1} (the middle white and blue velocity ranges in Fig. 2), shown in Fig. 3b, is dominated by the strongest emission from the Western region, but is otherwise relatively free from emission from the central plane (i.e., $b \sim 0^\circ$). On the other hand, the map shown in Fig. 3c, integrated from -60 to -40 km s^{-1} (the middle white and red velocity

ranges in Fig. 2) is much brighter near the RCW 106 H II region and has a diffuse filamentary component in the western region.

The H I emission in Figs. 3d-f does not appear to correlate very well with either ^{12}CO or 21 cm continuum emission, indicating that star formation activity does not correlate with this extended phase of the gas. However, in Figures 3d-e, H I seems to form in the outer envelope of the MCCs.

We have integrated the ^{12}CO , ^{13}CO , and H I data cubes in Galactic latitude (from -0.5° to 0.5°) to produce position-velocity ($l - V$) diagrams (Fig. 4). The main emission in the $l - V$ maps is from -72 km s^{-1} to -35 km s^{-1} as in the averaged spectra (Fig. 2). Another feature of strong though less prominent emission is from -112 km s^{-1} to -80 km s^{-1} at low l (western end). This is detached from the lower velocity structure supporting our division of the emission into two different complexes: in the East is the RCW 106 MCC spanning the velocity range from -72 to -40 km s^{-1} , the West is the complex MCC $331.0+0.0$ ($V_{LSR} = -90 \text{ km s}^{-1}$) (hereafter referred to with the informative name MCC331-90) spanning the velocity range from -112 to -80 km s^{-1} .

3.3. Insight from thermal dust emission

Figure 5 shows images of the thermal dust emission obtained in the mid-IR by *Spitzer* and in the far-IR and submillimeter by *Herschel* (Sect. 2.3).^{xix} These provide insight into the dust content, cloud morphology, and radiation field. In particular, data at $24 \mu\text{m}$ (Fig. 5a) allow us to trace local dust heating from the UV photons from young OB stars. Far-IR and submillimeter data probe cooler dust as well, both in the cloud and outside, and away from the influence of OB stars (Figures 5b-c).

The morphology of far-IR emission is generally similar to the CO emission (Fig. 3) suggesting that the gas and dust coexist within the MCCs. We also detect infrared dark clouds (IRDCs), seen as absorption in the mid-IR data but as emission in the far-IR data. These IRDCs are potential sites of massive star formation (Hennebelle et al. 2001; Rathborne et al. 2006; Simon et al. 2006; Peretto et al. 2010; Nguyen Luong et al. 2011a). In the dust emission at all wavelengths we see two main concentrations of dust at 331° and 333° whose detailed morphology matches well with that in the angled structures seen in the radio continuum and in ^{12}CO . This correlation indicates that both the 21 cm continuum and the dust heating are generated by the massive stars in the RCW 106 and MCC331-90 MCCs. The *Herschel* far-IR data also reveal finger-like protrusions at the bottom of the structure linked to MCC331-90. These features are plausibly formed by radiation pressure from numerous OB stars in the local interstellar medium (e.g., Krumholz & Matzner 2009; Gritschneider et al. 2010; Tremblin et al. 2013).

In summary, the dust emission data from $8-500 \mu\text{m}$ confirm that this region has two distinct MCCs that are both extremely active in forming massive stars, including hosting a young stellar cluster.

^{xix} Emission from Polycyclic Aromatic Hydrocarbons (PAHs) at $8 \mu\text{m}$ (not shown here) is also prominent in massive star forming regions (Peeters et al. 2004).

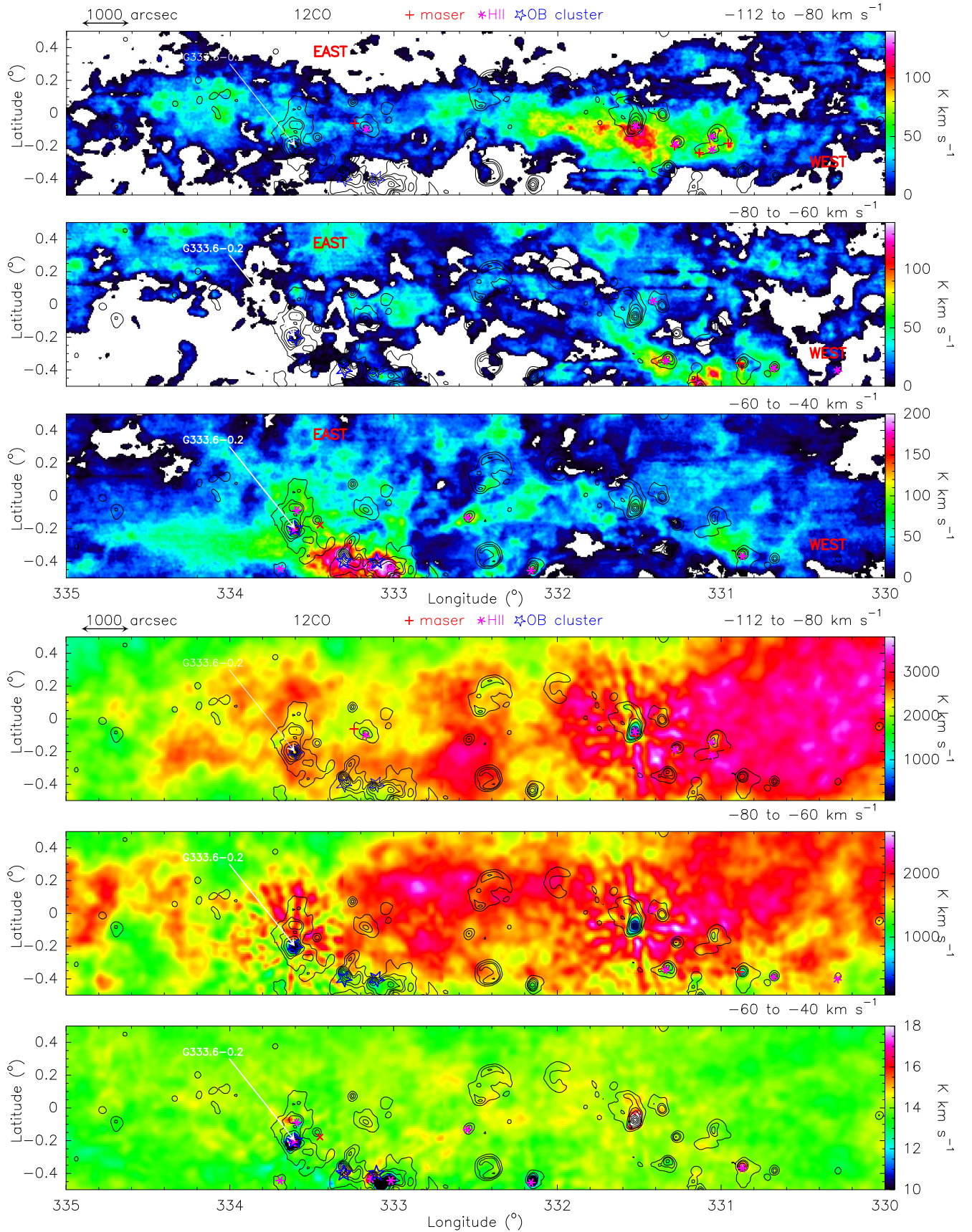


Figure 3. Upper – ^{12}CO integrated map for (a): -112 to -80 km s^{-1} ; (b): -80 to -60 km s^{-1} ; (c): -60 to -40 km s^{-1} . The black contours are from the 21 cm continuum emission in Fig. 1 with levels of 0.2, 0.6, 1, and 2 Jy beam^{-1} . As in Fig. 1 positions of cataloged OH masers and H II regions are marked, but now only in the map with the appropriate velocity range. OB clusters are marked on all panels. Lower – H I integrated maps ((d), (e), and (f)) for the same velocity ranges. The black contours are the ^{12}CO emission from the corresponding panels above with levels in increments of 20 K km s^{-1} from 10 to 90 K km s^{-1} for (d) and (e) and 10 to 150 K km s^{-1} for (f).

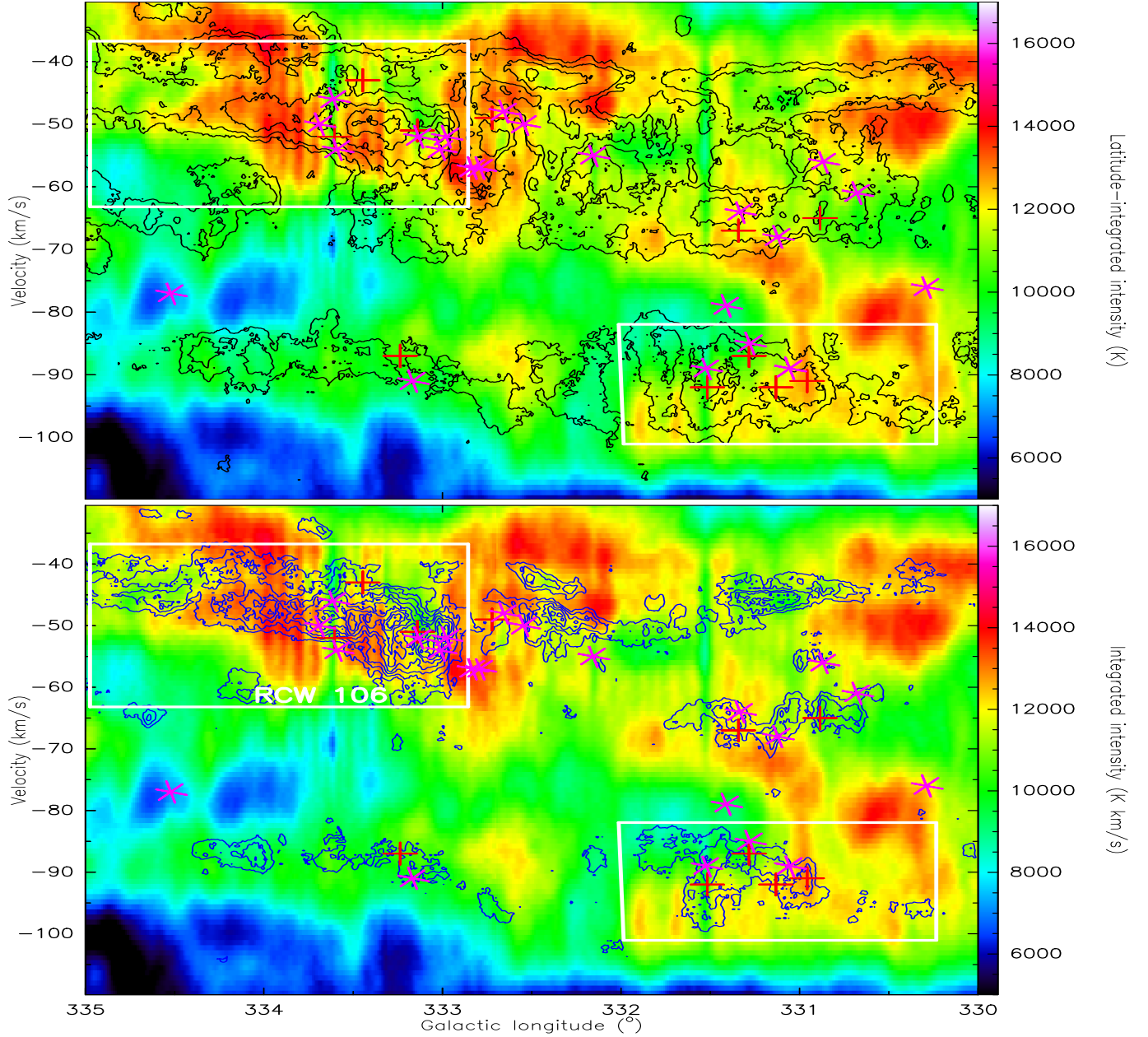


Figure 4. H I (color), ^{12}CO (black contour, upper panel), and ^{13}CO (blue contour, lower panel) position-velocity diagrams integrated from $b = -0^\circ.5$ to $b = 0^\circ.5$. As in previous figures, red crosses represent OH masers and magenta asterisks represent H II regions. The brightest 21 cm continuum sources in this region are at $l = 331^\circ.5$ and $l = 333^\circ.6$ (see Fig. 1 and Fig. 3). H I absorption against these sources results in vertical bands of relatively low (green) net H I emission cutting through higher intensity (yellow, red) regions for the entire velocity range corresponding to foreground gas.

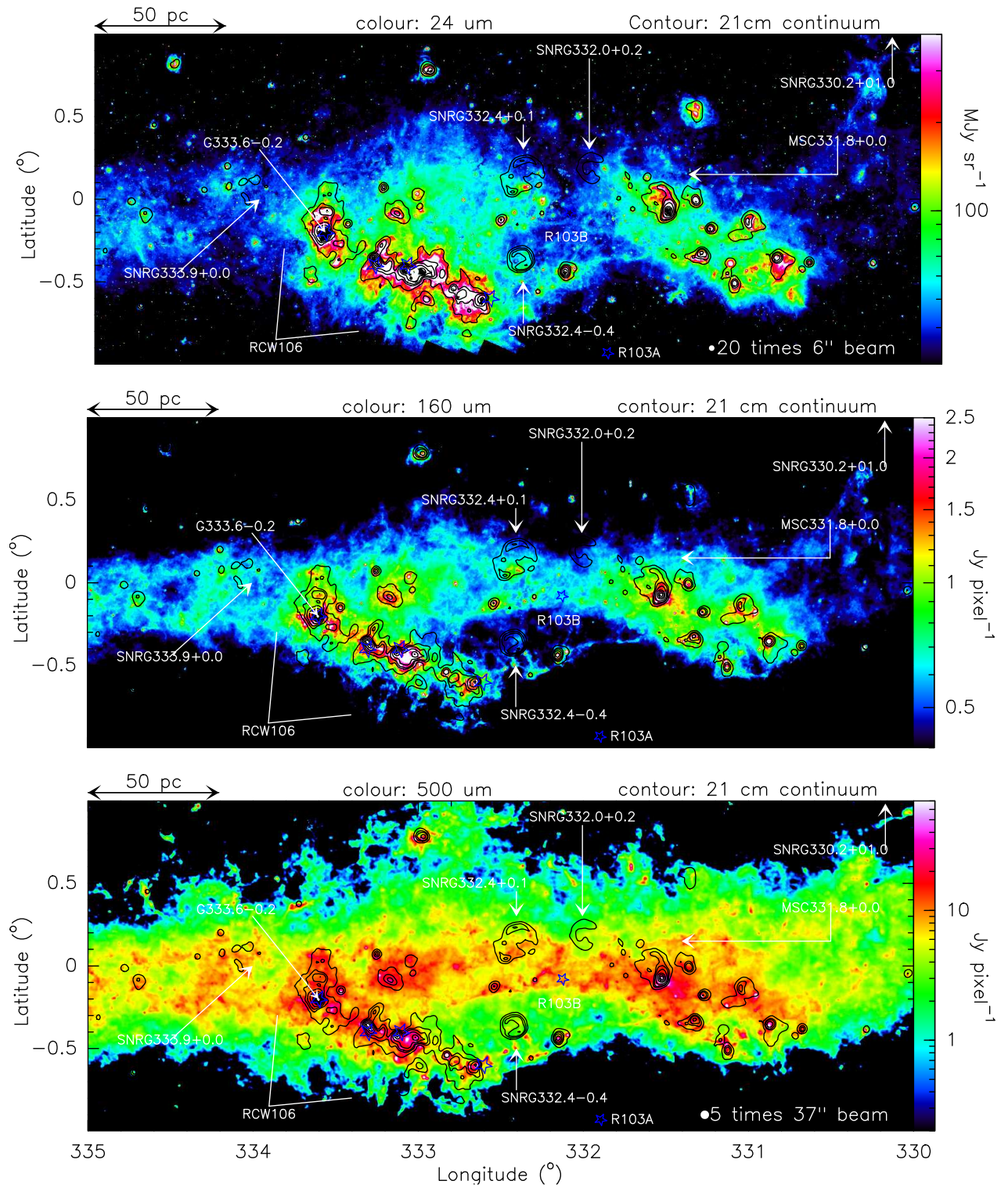


Figure 5. Dust emission (colour) from *Spitzer* 24 μm (Top), *Herschel* 160 μm (Middle), and *Herschel* 500 μm (Bottom), overlaid with 21 cm continuum emission contours (black). Blue stars mark the locations of bright OB clusters.

4. DISTANCES AND LOCATION OF THE OF RCW 106 AND MCC331-90 COMPLEXES

As shown in Fig. 2, the RCW 106 molecular cloud complex has two peaks centered at -48 and -63 km s^{-1} , whereas the MCC331-90 molecular cloud complex has only one V_{LSR} peak at ~ -90 km s^{-1} . We calculate the kinematic distances using the Galactic rotation curve of Reid et al. (2009), following the approach of Roman-Duval et al. (2009). For RCW 106 and MCC331-90, we obtain near distances of 3.3-4.1 kpc and 4.6-6.0 kpc, respectively, in contrast to far distances 10.2-12 kpc and 8.5-10 kpc, respectively. The far-distance solutions are very unlikely. First, at a distance of 11 kpc the MCC dimension would be ~ 200 pc, tripled the actual size calculated from the near solution. Second, the mass of RCW 106 would be a $\sim 10^7 - 10^8 M_{\odot}$, as massive as the CMZ. Furthermore, at a Galactic latitude of -1° it would imply that these MCCs are ~ 300 pc off the Galactic mid-plane, which seems implausible even for the thick disc. The near kinematic distance to the RCW 106 complex is also consistent with the photometric distance estimates to the RCW 106 OB cluster of 3.6 kpc (Moisés et al. 2011).

The 11 OH maser emission found by Caswell et al. (1980) lie in the spatial and velocity range of either the RCW 106 or MCC331-90 complex (see Figs. 1, 3 and 4), except for one source that lies in the spatial range of RCW 106 with an offset of ~ 40 km s^{-1} in V_{LSR} . The average near kinematic distances of the OH masers also coincide with those of these two MCC, therefore confirm our argument for near kinematic distance. (Jones & Dickey 2012) resolved the distance ambiguities for the RCW 106 and MCC331-90 complexes using H I absorption and found that more than 75% have near distances. Among these, 15 are assigned the near distances and four are uncertain.

To be consistent with the measurements from other methods in the literature (i.e., Bains et al. 2006; Moisés et al. 2011), we adopt 3.6 kpc as the distance to RCW 106. We also conclude that separation into two main molecular structures is physically meaningful, with both connected to signposts of massive star formation such as OH masers or H II regions. Hereafter, we adopt a distance of 3.6 kpc to the RCW 106 complex and 5 kpc to the MCC331-90 complex.

With our calculated distances for these MCCs, we can infer their locations in the Milky Way (Fig. 6). Based on models of the Galaxy (Georgelin & Georgelin 1976; Rodriguez-Fernandez & Combes 2008; Reid et al. 2009), RCW 106 can be placed in the nearby Scutum-Centaurus arm, the major arm of the Galaxy, while MCC331-90 is in the less prominent Norma arm.

The Scutum-Centaurus arm, a counterpart to the Perseus arm (Fig. 6), is characterized by a high fraction of dense gas (Sakamoto et al. 1997; Russeil et al. 2005) which may be the reason why the most massive Young Massive Clusters (YMCs) such as Westerlund 1, RSGC 1, RSGC 3 (Portegies Zwart et al. 2010), and the ministarburst W43 (Nguyen Luong et al. 2011b) are found therein. The $\ell - V$ diagram of the CO and H II emission shows a gradient toward the RCW 106 H II region (see upper dashed white line in Fig. 4) that might reflect a velocity gradient along the Scutum-Centaurus

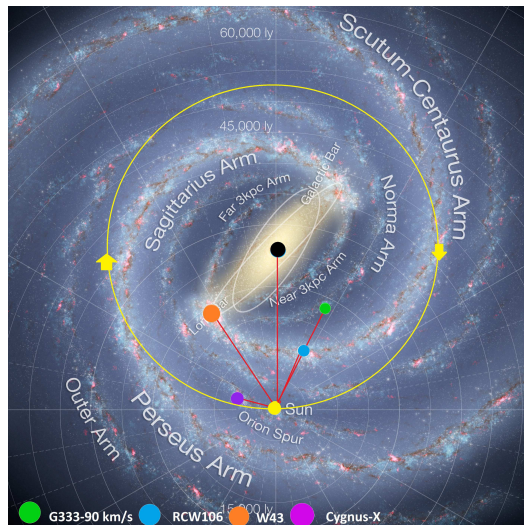


Figure 6. Artist's rendition of the Milky Way seen face-on by Robert Hurt of the *Spitzer* Science Centre with advice from Robert Benjamin from the University of Wisconsin-Whitewater. Colored dots mark the positions of GMCs, except for the black dot which marks the Galactic center. The RCW 106 complex is at $l = 333^{\circ}0$ and has a distance of 3.6 kpc from the Sun, while MCC331-90 is at $l = 331^{\circ}8$ and a distance of 5 kpc. Here it becomes obvious that the two GMCs are separate and actually part of different spiral arms.

arm toward the RCW 106 complex.

Although the Norma arm, a counterpart to the Sagittarius arm (Fig. 6), has less active star formation overall, MCC331-90 is known to host the luminous and efficient massive star forming cloud G331.5-0.1 (Merello et al. 2013a,b).

5. MASSES AND MASS SURFACE DENSITIES OF THE RCW 106 AND MCC331-90 COMPLEXES

We obtain the mass from $W(^{12}\text{CO})$, the ^{12}CO spectrum integrated over the velocity range -80 to -40 km s^{-1} for RCW 106 and -112 to -80 km s^{-1} for MCC331-90. The molecular hydrogen column density is from $N_{\text{H}_2} = X \times W(^{12}\text{CO})$, with $X = 1.8 \times 10^{20}$ $\text{cm}^{-2} \text{K}^{-1} \text{km s}^{-1}$ (Dame et al. 2001). This X factor is close to the value of 1.9×10^{20} $\text{cm}^{-2} \text{K}^{-1} \text{km s}^{-1}$ derived for the Perseus molecular arm from the diffuse gamma-ray emission (Abdo et al. 2010) and is lower than the value of 2.75×10^{20} $\text{cm}^{-2} \text{K}^{-1} \text{km s}^{-1}$ used for W43 and Cygnus X in Schneider et al. (2006) and Nguyen Luong et al. (2011b). Although X is uncertain because of the optical depth, metallicity, and excitation conditions, the mass estimates are probably accurate to a factor of two. The mass M_{total} in an area A_{cloud} would then be $M_{\text{total}} = N_{\text{H}_2} \times A_{\text{cloud}} \times \mu_{\text{H}_2} m_{\text{H}}$ where $\mu_{\text{H}_2} = 2.8$ is the mean H_2 molecular weight and m_{H} is the H atomic mass.

We use the ^{12}CO integrated intensity maps to define the extent of each cloud and adopt a rectangular shape that covers the main extent of the cloud (see Fig. 3) which is then used to calculate A using the assumed kinematic distance. The areas of the two clouds are 2.6×10^4 pc^2 and 2.2×10^4 pc^2 , which yield effective diameters of 183 and 137 pc, respectively. However, we integrate only within the contour $N_{\text{H}_2} = 5 \times 10^{22}$ cm^{-2} (corresponding to $W(^{12}\text{CO}) = 277 \text{K km s}^{-1}$) to minimize the effects of the foreground and background emission. This yields

Table 2
Properties of the two molecular cloud complexes in comparison with other star-forming complexes

Complex	A_{cloud}^a (pc ²)	D^b (pc)	Vel. range ^c (km s ⁻¹)	d^d (kpc)	M^e (M _⊙)	Σ_{gas}^f (M _⊙ pc ⁻²)	σ^g (km s ⁻¹)	M_{vir}^h (M _⊙)	α_{vir}^i	Σ_{SFR}^j (M _⊙ yr ⁻¹ kpc ⁻²)
RCW 106	2.6×10^4	183	-80 to -40	3.6	$5.9 \pm 1.77 \times 10^6$	221.2	4.5	2.1×10^6	0.35	0.15–0.3–(0.3–2.3) ^k
MCC331–90	2.2×10^4	167	-112 to -80	5.0	$2.8 \pm 0.84 \times 10^6$	127.1	3.7	1.4×10^6	0.5	-
<Gould Belt> ^l	32.4^1	6.4^1	-	0.27^1	3.0×10^3	79.3^1	-	-	-	-
W43 ^m	1.5×10^4	~ 140	80 to 100	6.0	7.1×10^6	473	9.3	2.4×10^7	0.3–0.5 ^m	0.65–(6.5) ^k
Cygnus X ^{m,n}	2.0×10^4	~ 160	-10 to 20	1.7	5.0×10^6	250	4.2	5.5×10^6	0.9	-
CMZ ^{m,o}	9.6×10^4	~ 350	-225 to 225	8.5	3.0×10^8	3125	-	-	-	-

^aSurface areas calculated at adopted distances. ^bEquivalent diameter $D = \sqrt{A_{\text{cloud}}/\pi}$. ^cMain velocity range of the structure. ^dAdopted distance. ^eMass calculated from the CO emission using an X of 1.8×10^{20} cm⁻² K⁻¹ km s⁻¹ except for Gould Belt clouds being calculated from dust extinction map and for CMZ from thermal dust emission. ^fMass surface density $\Sigma_{\text{gas}} = M/A_{\text{cloud}}$. ^gVelocity dispersion $\sigma = \Delta V_{\text{FWHM}}/\sqrt{8\ln 2}$. ^hVirial mass. ⁱ3D virial parameter described by $\alpha_{\text{vir}} = M_{\text{vir}}/M_{\text{total}}$. ^jStar formation rate (SFR) density. ^kFirst numbers are the past SFR density and bold numbers in brackets are the future SFR density (see Sect. 7). ^lAverage of 20 large molecular clouds from *Spitzer* cores to disks and Gould Belt surveys (Heiderman et al. 2010). ^mFrom Nguyen Luong et al. (2011b) with X factor scaled to 1.8×10^{20} cm⁻² K⁻¹ km s⁻¹. ⁿFrom Schneider et al. (2006) using ¹³CO. ^oFrom Dahmen et al. (1998) using C¹⁸O.

masses $5.9 \times 10^6 M_{\odot}$ and $2.8 \times 10^6 M_{\odot}$ and approximate surface densities 220 and 130 M_⊙ pc⁻² for the RCW 106 and MCC331–90 complexes, respectively. We estimate an uncertainty of 30% because of the background and foreground confusion as well as optical depth. The properties are collected in Table 2.

The total clump mass deduced from measurements of ¹³CO (Bains et al. 2006), mm continuum (Mookerjee et al. 2004), and far-IR (Karnik et al. 2001) toward RCW 106 is only 10–30% of our estimate, for two reasons. First, the previous measurements estimate only the clump mass whereas we calculate the total gas mass which includes in addition the more diffuse large-scale structure.^{xx} Second, while these three studies focus in on the ~ 1 square degree area surrounding the RCW 106 cluster, we are studying a region almost five times larger.

Heiderman et al. (2010) investigated 20 low-mass star-forming clouds in the Gould Belt region and found an average mass ~ 3000 M_⊙, area 32 pc², and surface density of 80 M_⊙ pc⁻² (Table 2). Compared to these, the two complexes studied here are ~ 100 times larger in area and yet because the masses are so much higher the mass surface densities are also higher. In reference to a typical massive star forming region such as Cygnus X, the mass surface density of RCW 106 is comparable, while MCC331–90 is about half. But compared to the mass surface densities of the extreme massive star forming regions such as W43 or CMZ molecular cloud, the values here are lower still (Table 2).

6. DYNAMICS OF RCW 106 AND MCC331–90 COMPLEXES

We fit a single Gaussian profile to the spectra of the RCW 106 and MCC331–90 MCCs and obtains FWHM widths of 10.6 and 8.7 km s⁻¹ corresponding to a one-dimensional (1D) velocity dispersion $\sigma = \Delta V_{\text{FWHM}}/\sqrt{8\ln 2}$ of 4.5 and 3.7 km s⁻¹, respectively. This value is within the typical range for MCCs found in other observations (W43, Nguyen Luong et al. 2011a; Cygnus X, Schneider et al. 2006) or in simulations of molecular clouds in spiral arms (Dobbs & Pringle 2013).

First, to compare with other complexes, we estimate the gravitational instability criterium for the RCW 106

^{xx} The ratio of total clump mass to the total gas mass can also be considered as the clump formation efficiency, as elaborated further in Section 7.

complex using the spherical approximation and assuming that its effective radius R_{sph} (half the diameter D in Table 2) as:

$$\alpha_{\text{vir}} = 5 \times \frac{R_{\text{sph}} \sigma_{1D}^2}{GM} = \frac{M_{\text{vir}}}{M_{\text{total}}}. \quad (1)$$

Both complexes have low *spherical virial parameters* (0.35 for RCW 106 and 0.5 for MCC331–90; see Table 2).

However, since the global structure of RCW 106 complex is filamentary with an aspect ratio $r = \frac{l}{w} = \frac{180 \text{ pc}}{50 \text{ pc}} = 3.6$, we use the gravitational instability criterium of an infinite-length isothermal gas cylinder (Ostriker 1964; Inutsuka & Miyama 1992; see also Dibai 1958; Ozernoi 1964). This model defines a critical line mass (mass per unit length, $M_{\text{line,crit}}$ solely on the sound speed c_s , above which the filamentary cloud is unstable against collapsing. For a large molecular cloud complex, the internal motion depends also on turbulence in addition to its thermal motion, therefore we assume that the apparent "sound speed c_s " equals the observed line width ΔV (similar as in Dobashi et al. 2014). We calculate the *filamentary virial parameter* $\alpha_{\text{vir}}^{\text{fil}}$, defined as:

$$\alpha_{\text{vir}}^{\text{fil}} = \frac{M_{\text{line,crit}}}{M_{\text{line,gas}}} = \frac{2c_s^2/G}{M/l} = \frac{465\Delta V [\text{M}_{\odot} \text{ pc}^{-1}]}{M/l [\text{M}_{\odot} \text{ pc}^{-1}]}. \quad (2)$$

The total gas mass M is integrated over the RCW 106 and MCC331–90 filamentary clouds with length l and width w . We obtain low $\alpha_{\text{vir}}^{\text{fil}}$ of 0.15 for RCW 106 and 0.26 for MCC331–90, which confirm that these two complexes are indeed gravitationally unstable.

While the gravitationally unstable states of these clouds are certain, a more detailed investigation is needed to justify their origin. They might be caused by strong dynamical affects related to their locations spread along the respective spiral arms (see Section 4) and/or feedback from the vigorous burst of star formation within (see Section 7).

7. A BURST OF STAR FORMATION IN THE RCW 106 COMPLEX

Ly α continuum photons from young stars create H II regions quantifiable by free-free emission. We find 30 H II regions hosting O- or B-type stars in the RCW 106 complex (Table 3). We checked the CO and H I V_{LSR} of

gas surrounding these H II regions and confirmed that they are in the velocity range of the RCW 106 complex. We estimated the radio continuum flux density S_ν of each H II region by aperture photometry on the the 21 cm map within the contour defined by the 3σ noise level (see Appendix A). An average background level of ~ 0.09 Jy beam $^{-1}$ was derived by averaging the intensity within a surrounding empty region. Following Mezger & Henderson (1967), the number of Ly α continuum photons powering an ionization-bounded region can be computed using

$$\frac{N_{\text{Ly}\alpha}}{8.9 \times 10^{46} \text{ s}^{-1}} = \frac{S_\nu}{\text{Jy}} \left[\frac{\nu}{\text{GHz}} \right]^{0.1} \left[\frac{T_e}{10^4 \text{ K}} \right]^{-0.45} \left[\frac{d}{\text{kpc}} \right]^2. \quad (3)$$

where $T_e = 8000$ K (Wilson et al. 2012) is the electron temperature, $\nu = 1.42$ GHz is the observing frequency, and d is the distance to the H II region. The distance is 3.6 kpc for the RCW 106 complex (see Sect. 4).

If we assume that a single main-sequence star dominates the ionization,^{xxi} we can then use $N_{\text{Ly}\alpha}$ to obtain the spectral type (Thompson 1984; Martins et al. 2008). The estimated types are O7V or earlier.

Given that an O7 star with mass $\sim 25 M_\odot$ emits $N_{\text{Ly}\alpha} = 5 \times 10^{48} \text{ s}^{-1}$ (Martins et al. 2005), we can estimate an upper limit on the number of stars that have spectral type O7 or earlier in each H II region of the RCW 106 cloud complex (Table 3); in total, there are up to 54 O7 stars currently formed. Assuming that the stellar masses in the RCW 106 complex follow the Salpeter Initial Mass Function (IMF) $dN/dm = A \times m^{-2.35}$ (Salpeter 1955) and have a minimum cut-off mass of $0.08 M_\odot$ and maximum cut-off mass of $50 M_\odot$, the total stellar mass of RCW 106 will then be

$$M_* = A \int m^{-\alpha} dm = A \times \frac{m_{\text{max}}^{-0.35} - m_{\text{min}}^{-0.35}}{-0.35}. \quad (4)$$

The normalization factor A can be calculated from the total number of O7 stars calculated above by the approximation that this is the total number of all stars with masses in the range of 25 to $50 M_\odot$ so that

$$N_{m_1}^{m_u} = A \times \frac{m_u^{-1.35} - m_1^{-1.35}}{-1.35}. \quad (5)$$

To gauge the uncertainty, we varied the upper mass limit to $100 M_\odot$ and allowed for a dispersion of ± 5 stars in the estimate of the total number of O7 stars. Finally, we obtain a value of $\sim 7761_{-719}^{+2753}$ for the factor A and a total stellar mass of $\sim 48_{-4}^{+17} \times 10^3 M_\odot$. Replacing the Salpeter IMF by the Kroupa IMF (Kroupa 2001) lowers the total stellar mass but it is within the calculated uncertainty.

7.1. The immediate past

Because an O7V star with a mass of $25 M_\odot$ has a lifetime of $\sim 2 \times 10^5$ yr starting from its first appearance on the main-sequence diagram, we can calculate the star formation efficiency $\epsilon_{\text{cloud}}^{\text{past}}$, the star formation rate

^{xxi} Of course, it is possible that the ionization is produced by a combination of several stars of somewhat later spectral type; however, usually only the brightest star dominates the output of ionizing photons.

$SFR_{\text{cloud}}^{\text{past}}$, and the SFR density $\Sigma_{\text{SFR,cloud}}^{\text{past}}$ of the entire RCW 106 cloud complex for this ‘‘past’’ time interval as

$$\epsilon_{\text{cloud}}^{\text{past}} = \frac{M_*}{M_{\text{cloud}} + M_*} = 0.008_{-0.003}^{+0.004}, \quad (6)$$

$$SFR_{\text{cloud}}^{\text{past}} = \frac{M_*}{2 \times 10^5 \text{ yr}} = 0.25_{-0.023}^{+0.09} M_\odot \text{ yr}^{-1}, \quad (7)$$

$$\Sigma_{\text{SFR,cloud}}^{\text{past}} = \frac{SFR}{A_{\text{cloud}}} = 9.5_{-0.9}^{+3.4} M_\odot \text{ yr}^{-1} \text{ kpc}^{-2}. \quad (8)$$

with the total stellar mass $M_* = 4.8 \times 10^4 M_\odot$, the total gas mass $M_{\text{cloud}} = 5.9 \times 10^6 M_\odot$ calculated over an area of $A_{\text{cloud}} = 2.6 \times 10^4 \text{ pc}^2$.

The estimated $\epsilon_{\text{cloud}}^{\text{past}}$ is in the middle of the range for GMCs, 0.002–0.2, as derived from the ionizing flux of young stars (Murray 2011). However, the SFR density of RCW 106 is high and for its surface density of $220 M_\odot \text{ pc}^{-2}$ (Sect. 5) it is well above the trend in the Schmidt–Kennicutt relation (see Fig. 7). This shows that RCW 106 has been very active in forming massive stars during the last 2×10^5 yr.

7.2. The immediate future

The large amount of gas remaining in this complex suggests that the burst of star formation activity in the RCW 106 molecular cloud complex might not yet be finished. We investigated this by estimating the future star-formation activity using the dense clump and core populations.

First, we make an assumption that the dense clump mass of $2.2 - 2.7 \times 10^5 M_\odot$ derived from ^{13}CO line emission (Bains et al. 2006) or 1.2 mm continuum emission (Wong et al. 2008) represents the clump mass of the entire RCW 106 complex. This assumption is justified since most of the dense gas concentrates in the region considered by Bains et al. (2006) and Wong et al. (2008) (see for example Figure 5). We estimate the clump formation efficiency, $\epsilon_{\text{cloud} \rightarrow \text{clump}}$,^{xxii} as the ratio of the total clump mass to the total cloud mass (Eden et al. 2012, 2013; Louvet et al. 2014):

$$\epsilon_{\text{cloud} \rightarrow \text{clump}} = \frac{M_{\text{clump}}}{M_{\text{cloud}}} \sim 0.042 \pm 0.013. \quad (9)$$

The estimated $\epsilon_{\text{cloud} \rightarrow \text{clump}}$ of the RCW 106 complex is about 10 times higher than that of the famous massive star-forming region Cygnus X and almost equal to that of W43 (Nguyen Luong et al. 2011b). Thus the RCW 106 complex is forming massive clumps almost as efficiently as the W43 star forming region despite the mass surface density of RCW 106 being four times lower.

Secondly, a cloud’s efficiency at converting mass into dense clumps subsequently affects the star formation efficiency (Eden et al. 2012; Louvet et al. 2014). If the dense clumps ($r \sim 1$ pc) in the RCW 106 complex form dense cores ($r \sim 0.1$ pc) with a mass transfer efficiency $\epsilon_{\text{clump} \rightarrow \text{core}}$, and dense cores will form protostars with a mass transfer efficiency $\epsilon_{\text{core} \rightarrow *}$, the future star formation efficiency of the entire cloud will be

$$\epsilon_{\text{cloud} \rightarrow *} = \epsilon_{\text{cloud} \rightarrow \text{clump}} \times \epsilon_{\text{clump} \rightarrow \text{core}} \times \epsilon_{\text{core} \rightarrow *}. \quad (10)$$

^{xxii} This parameter is also known as the compactness of a molecular cloud (Nguyen Luong et al. 2011b).

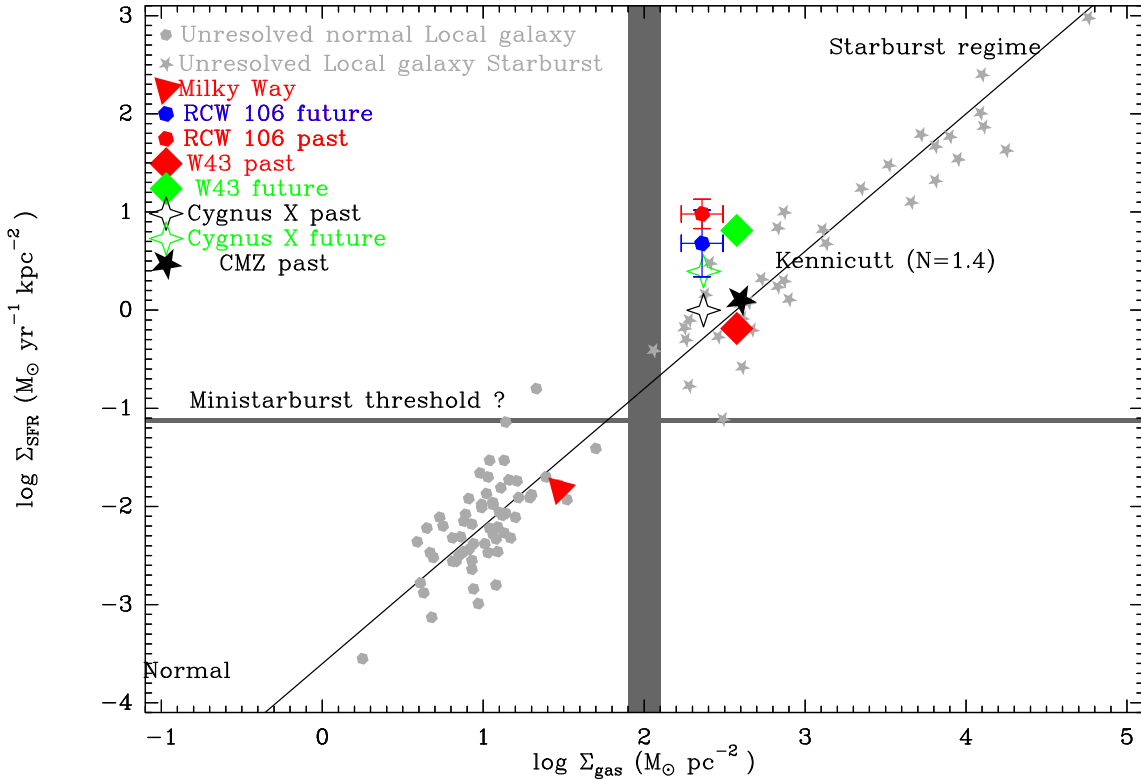


Figure 7. The Schmidt-Kennicutt relation between the star formation rate (SFR) density and gas surface density extending from normal spiral galaxies to starbursts (Kennicutt 1998). Also plotted are values for the average Milky Way, the immediate past and future of the RCW 106 complex, the past and future SFR density of the W43 complex, the past and future SFR density of the Cygnus X complex, and the past SFR density of the CMZ complex.

If we adopt typical values $\epsilon_{\text{clump} \rightarrow \text{core}} \sim 0.1 - 0.3$ (Parmentier & Pfalzner 2013; Louvet et al. 2014) and $\epsilon_{\text{core} \rightarrow *}$ $\sim 0.3 - 0.8$ (Alves et al. 2007; Parmentier & Pfalzner 2013; Myers 2014), we will have a future $\epsilon_{\text{cloud} \rightarrow *}$ $\sim 0.004 \pm 0.004$.

Because the massive protostellar phase has a timescale of $\sim 2 \times 10^5$ yr (Motte et al. 2007; Russeil et al. 2012), similar to OB stars, we calculate the “future 2×10^5 yr” (“future”) SFR and SFR density as

$$SFR_{\text{cloud}}^{\text{future}} = \frac{\epsilon_{\text{cloud} \rightarrow *}}{2 \times 10^5 \text{ yr}} M_{\text{cloud}} = 0.12 \pm 0.1 M_{\odot} \text{ yr}^{-1} \quad (11)$$

and

$$\Sigma_{\text{SFR, cloud}}^{\text{future}} = \frac{SFR_{\text{cloud}}^{\text{future}}}{A_{\text{cloud}}} = 4.8 \pm 3.8 M_{\odot} \text{ yr}^{-1} \text{ kpc}^{-2}. \quad (12)$$

This SFR density and the surface density also combine to place the RCW 106 complex in the starburst regime of the Schmidt-Kennicutt relation (Kennicutt 1998; see Fig. 7). It should be possible to refine and confirm the future SFR density of the RCW 106 complex by counting the massive dense cores identified using the *Herschel* data. This will be the topic of a subsequent paper.

These SFR densities are similar to the future SFR density of W43 and higher than that of Cygnus X, reinforcing the conclusion that RCW 106 is undergoing a ministarburst at present. The similarity between past and future SFR densities implies that this ministarburst event is not yet finished but is in the declining phase. It is also much higher than the SFR density of CMZ, the region of the

galactic plane within a few degrees of the Galactic centre, well-known for its inefficiency in star formation despite being 100 times more massive than RCW 106 complex (Immer et al. 2012; Kruijssen et al. 2014).

While this is consistent with the large mass reservoir still available in the RCW 106 complex, there are still questions outstanding including what the final conversion efficiency will be and its relationship to the virial parameter (Section 6).

7.3. Uncertainties

The calculations in Sections 7.1 and 7.2 should involve the general uncertainties from the assumptions of the IMF, the timescales, and the mass transfer efficiencies. Several authors suggest that the IMF of the extreme star-formation environment is top-heavy (Stolte et al. 2002, 2005; Chabrier et al. 2014). However, the validity of this statement is still largely debated (Kim et al. 2006; Brandner et al. 2008). If we use an IMF with a steeper slope, the SFR likely increases by about 20%. We assume a burst period timescale of 2×10^5 yr, which might have variations within a factor of two; but this is the most appropriate assumption since this is the measured timescale of an OB star (Martins et al. 2005) and an MDC (Motte et al. 2007). The third uncertainty is the mass transfer efficiencies from clouds to clumps, to cores and to stars. Our assumptions of these quantities are the average results of the current state-of-the-art theoretical and observational studies, therefore the true values might vary at most 10%–30%. We already take these three uncertainties into account in our calculations.

The uncertainties from measurements of Ly α photons

and the clump mass are low since we focus only on the brightest regions in the radio continuum map (in case of estimating the Ly α photons) and in millimeter continuum or ^{13}CO maps (in case of estimating the clump mass). For the later case, the clump mass is verified with an independent measurement from NH_3 emission (Lowe et al. 2014).

8. CONCLUSIONS

Using a combination of data sets, we have defined and characterized two MCCs in the general direction of the RCW 106 OB cluster, and we have labelled them the RCW 106 and MCC331–90 complexes. Their properties are summarized as follows

- The V_{LSR} for gas in the RCW 106 complex ranges between -40 and -80 km s^{-1} and the V_{LSR} for MCC331–90 is between -80 and -112 km s^{-1} . Both complexes have velocity dispersions comparable to that of Cygnus X ($\sigma=4.2 \text{ km s}^{-1}$) but smaller in comparison to W43 ($\sigma=9.3 \text{ km s}^{-1}$), which is right in the Galactic bar and a known turbulent area.
- OH masers and H II region studies confirmed the near kinematic distances of 3.6 kpc for RCW 106 and 5 kpc for MCC331–90. This places the RCW 106 molecular cloud complex in the Scutum–Centaurus arm and MCC331–90 in the Norma arm.
- The RCW 106 complex has a mass of $5.9 \times 10^6 M_{\odot}$ and a surface density of $\sim 220 M_{\odot} \text{ pc}^{-2}$, whereas the MCC331–90 complex has a mass of $2.8 \times 10^6 M_{\odot}$ and surface density of $\sim 130 M_{\odot} \text{ pc}^{-2}$. These surface densities are higher compared to the average Gould Belt cloud ($\sim 70 M_{\odot} \text{ pc}^{-2}$) and the surface areas are 10^3 times larger.
- These two complexes are of comparable size ($d \sim 180 \text{ pc}$) but have less mass in comparison to other large GMCs such as W43 and Cygnus X. Hence, the surface densities are smaller.
- The virial parameters are greater than unity, indicating that they are gravitationally unbound.
- Using the 21 cm continuum, we separated the region into 31 subregions: 25 containing H II regions and 6 containing SNRs. We estimated that there are about 50 young O7V stars currently in the RCW 106 complex.
- For the RCW 106 molecular cloud complex, we derive a past global star formation efficiency, SFR, and SFR density and estimate values to quantify star formation in the near future. These values suggest that the RCW 106 complex is undergoing a ministarburst event.

Acknowledgements: H.N. is grateful for a CITA summer student internship. P.G.M. acknowledges support from the Canadian Space Agency and the Natural Sciences and Engineering Research Council of Canada. Nadia Lo’s postdoctoral fellowship is supported by CONICYT/FONDECYT postdoctorado under project No. 3130540.

REFERENCES

- Abdo, A. A., Ackermann, M., Ajello, M., et al. 2010, ApJ, 710, 133
- Alves, J., Lombardi, M., & Lada, C. J. 2007, A&A, 462, L17
- Bains, I., Wong, T., Cunningham, M., et al. 2006, MNRAS, 367, 1609
- Barnes, P., Muller, E., Indermuhle, B., et al. 2013, ApJ
- Brandner, W., Clark, J. S., Stolte, A., et al. 2008, A&A, 478, 137
- Bronfman, L., Alvarez, H., Cohen, R. S., & Thaddeus, P. 1989, ApJS, 71, 481
- Carey, S. J., Noriega-Crespo, A., Mizuno, D. R., et al. 2009, PASP, 121, 76
- Caswell, J. L. & Haynes, R. F. 1975, MNRAS, 173, 649
- Caswell, J. L., Haynes, R. F., & Goss, W. M. 1980, Australian Journal of Physics, 33, 639
- Chabrier, G., Hennebelle, P., & Charlot, S. 2014, ApJ, 796, 75
- Dahmen, G., Huttmeister, S., Wilson, T. L., & Mauersberger, R. 1998, A&A, 331, 959
- Dame, T. M., Hartmann, D., & Thaddeus, P. 2001, ApJ, 547, 792
- Dibai, E. A. 1958, Soviet Ast., 2, 226
- Dobashi, K., Matsumoto, T., Shimoikura, T., et al. 2014, ApJ, 797, 58
- Dobbs, C. L. & Pringle, J. E. 2013, MNRAS, 432, 653
- Dutra, C. M., Bica, E., Soares, J., & Barbuy, B. 2003, A&A, 400, 533
- Eden, D. J., Moore, T. J. T., Morgan, L. K., Thompson, M. A., & Urquhart, J. S. 2013, MNRAS, 431, 1587
- Eden, D. J., Moore, T. J. T., Plume, R., & Morgan, L. K. 2012, MNRAS, 422, 3178
- Fujiyoshi, T., Smith, C. H., Caswell, J. L., et al. 2006, MNRAS, 368, 1843
- Fujiyoshi, T., Smith, C. H., Moore, T. J. T., et al. 2005, MNRAS, 356, 801
- Georgelin, Y. M. & Georgelin, Y. P. 1976, A&A, 49, 57
- Grave, J. M. C., Kumar, M. S. N., Ojha, D. K., Teixeira, G. D. C., & Pace, G. 2014, A&A, 563, A123
- Green, D. A. 2009, Bulletin of the Astronomical Society of India, 37, 45
- Griffin, M. J., Abergel, A., Abreu, A., et al. 2010, A&A, 518, L3+
- Gritschneider, M., Burkert, A., Naab, T., & Walch, S. 2010, ApJ, 723, 971
- Heiderman, A., Evans, II, N. J., Allen, L. E., Huard, T., & Heyer, M. 2010, ApJ, 723, 1019
- Hennebelle, P., Pérault, M., Teyssier, D., & Ganesh, S. 2001, A&A, 365, 598
- Immer, K., Menten, K. M., Schuller, F., & Lis, D. C. 2012, A&A, 548, A120
- Inutsuka, S. & Miyama, S. M. 1992, ApJ, 388, 392
- Jackson, J. M., Rathborne, J. M., Shah, R. Y., et al. 2006, ApJS, 163, 145
- Jones, C. & Dickey, J. M. 2012, ApJ, 753, 62
- Jones, P. A., Burton, M. G., Cunningham, M. R., et al. 2012, MNRAS, 419, 2961
- Karnik, A. D., Ghosh, S. K., Rengarajan, T. N., & Verma, R. P. 2001, MNRAS, 326, 293
- Kennicutt, Jr., R. C. 1998, ApJ, 498, 541
- Kim, S. S., Figer, D. F., Kudritzki, R. P., & Najarro, F. 2006, ApJ, 653, L113
- Kroupa, P. 2001, MNRAS, 322, 231
- Kruijssen, J. M. D., Longmore, S. N., Elmegreen, B. G., et al. 2014, MNRAS, 440, 3370
- Krumholz, M. R. & Matzner, C. D. 2009, ApJ, 703, 1352
- Kuchar, T. A. & Clark, F. O. 1997, ApJ, 488, 224
- Kumar, M. S. N. 2013, A&A, 558, A119
- Lo, N., Cunningham, M., Bains, I., Burton, M. G., & Garay, G. 2007, MNRAS, 381, L30
- Lo, N., Cunningham, M. R., Jones, P. A., et al. 2009, MNRAS, 395, 1021
- Lo, N., Redman, M. P., Jones, P. A., et al. 2011, MNRAS, 415, 525
- Lockman, F. J. 1979, ApJ, 232, 761
- Louvet, F., Motte, F., Hennebelle, P., et al. 2014, A&A, 570, A15
- Lowe, V., Cunningham, M. R., Urquhart, J. S., et al. 2014, MNRAS, 441, 256
- Lynga, G. 1964, Meddelanden fran Lunds Astronomiska Observatorium Serie II, 141, 1
- Martins, F., Hillier, D. J., Paumard, T., et al. 2008, A&A, 478, 219
- Martins, F., Schaerer, D., & Hillier, D. J. 2005, A&A, 436, 1049

- McClure-Griffiths, N. M., Dickey, J. M., Gaensler, B. M., et al. 2005, *ApJS*, 158, 178
- McClure-Griffiths, N. M., Green, A. J., Dickey, J. M., et al. 2001, *ApJ*, 551, 394
- Mel’Nik, A. M. & Efremov, Y. N. 1995, *Astronomy Letters*, 21, 10
- Mercer, E. P., Clemens, D. P., Meade, M. R., et al. 2005, *ApJ*, 635, 560
- Merello, M., Bronfman, L., Garay, G., et al. 2013a, *ApJ*, 774, L7
- Merello, M., Bronfman, L., Garay, G., et al. 2013b, *ApJ*, 774, 38
- Mezger, P. G. & Henderson, A. P. 1967, *ApJ*, 147, 471
- Miyazaki, A. & Tsuboi, M. 2000, *ApJ*, 536, 357
- Moisés, A. P., Damineli, A., Figuerêdo, E., et al. 2011, *MNRAS*, 411, 705
- Molinari, S., Swinyard, B., Bally, J., et al. 2010, *A&A*, 518, L100+
- Mookerjea, B., Kramer, C., Nielbock, M., & Nyman, L.-Å. 2004, *A&A*, 426, 119
- Motte, F., Bontemps, S., Schilke, P., et al. 2007, *A&A*, 476, 1243
- Motte, F., Nguyen Luong, Q., Schneider, N., et al. 2014, *A&A*, 571, A32
- Murray, N. 2011, *ApJ*, 729, 133
- Myers, P. C. 2014, *ApJ*, 781, 33
- Nguyen Luong, Q., Motte, F., Hennemann, M., et al. 2011a, *A&A*, 535, A76
- Nguyen Luong, Q., Motte, F., Schuller, F., et al. 2011b, *A&A*, 529, A41+
- Ostriker, J. 1964, *ApJ*, 140, 1056
- Ozernoi, L. M. 1964, *Soviet Ast.*, 8, 137
- Parmentier, G. & Pfalzner, S. 2013, *A&A*, 549, A132
- Peeters, E., Spoon, H. W. W., & Tielens, A. G. G. M. 2004, *ApJ*, 613, 986
- Peretto, N., Fuller, G. A., Plume, R., et al. 2010, *A&A*, 518, L98+
- Poglitsch, A., Waelkens, C., Geis, N., et al. 2010, *A&A*, 518, L2+
- Portegies Zwart, S. F., McMillan, S. L. W., & Gieles, M. 2010, *ARA&A*, 48, 431
- Rathborne, J. M., Jackson, J. M., & Simon, R. 2006, *ApJ*, 641, 389
- Reid, M. J., Menten, K. M., Zheng, X. W., et al. 2009, *ApJ*, 700, 137
- Robitaille, T. P., Meade, M. R., Babler, B. L., et al. 2008, *AJ*, 136, 2413
- Rodgers, A. W., Campbell, C. T., & Whiteoak, J. B. 1960, *MNRAS*, 121, 103
- Rodriguez-Fernandez, N. J. & Combes, F. 2008, *A&A*, 489, 115
- Roman-Duval, J., Jackson, J. M., Heyer, M., et al. 2009, *ApJ*, 699, 1153
- Roussel, H. 2013, *PASP*, 125, 1126
- Russeil, D., Adami, C., Amram, P., et al. 2005, *A&A*, 429, 497
- Russeil, D., Zavagno, A., Adami, C., et al. 2012, *A&A*, 538, A142
- Sakamoto, S., Hasegawa, T., Handa, T., Hayashi, M., & Oka, T. 1997, *ApJ*, 486, 276
- Salpeter, E. E. 1955, *ApJ*, 121, 161
- Schneider, N., Bontemps, S., Simon, R., et al. 2006, *A&A*, 458, 855
- Simon, R., Rathborne, J. M., Shah, R. Y., Jackson, J. M., & Chambers, E. T. 2006, *ApJ*, 653, 1325
- Stolte, A., Brandner, W., Grebel, E. K., Lenzen, R., & Lagrange, A.-M. 2005, *ApJ*, 628, L113
- Stolte, A., Grebel, E. K., Brandner, W., & Figer, D. F. 2002, *A&A*, 394, 459
- Thompson, R. I. 1984, *ApJ*, 283, 165
- Tremblin, P., Minier, V., Schneider, N., et al. 2013, *A&A*, 560, A19
- Urquhart, J. S., Busfield, A. L., Hoare, M. G., et al. 2007, *A&A*, 461, 11
- Walsh, A. J., Hyland, A. R., Robinson, G., & Burton, M. G. 1997, *MNRAS*, 291, 261
- Wilson, T. L., Casassus, S., & Keating, K. M. 2012, *ApJ*, 744, 161
- Wong, T., Ladd, E. F., Brisbin, D., et al. 2008, *MNRAS*, 386, 1069

APPENDIX

A. 21 CM CONTINUUM SOURCES

In Fig. 1, we selected 31 rectangular subregions in the 21 cm continuum data in which there is significant emission. These are the “boxes” whose details are captured in Table 3.

Across the continuum image the background is rather similar, about ~ 0.09 Jy beam $^{-1}$, and contours are given starting at the 3σ noise level above the local background. We integrated the background-subtracted 21 cm intensity within the area defined by the 3σ noise contour. The flux densities range from 0.1 to 12 Jy and the sizes range from a few arcminutes to several hundred arcminutes. There is no apparent correlation of size and flux density. From these parameters and the distance, we have derived and tabulated the characteristics of the star formation in Table 3. Star formation in the RCW 106 complex is discussed in Section 7.

Because of the massive star formation across the region there are many H II regions. These can be classified according to their shapes: circular or irregular. The H II region around RCW 106 is classified separately as a giant H II region and the components are displayed in Figure 8. There are also several SNRs seen in projection on the region. These structures can be seen in magnified views of these “boxes” in Figs. 9–11 in the subsections below. Within each figure, the boxes are shown on the same angular scale, as labeled, with the box number at the lower left of each sub-image. The spatial locations and relationships of the boxes can be seen in Fig. 1. In all figures, except Fig. 11 for SNRs, a linear scale is also given, assuming a distance of 3.6 kpc, although the structures associated with MCC331–90 (Table 3) are at 5 kpc.

Table 3
Details of boxes and subregions as selected from the 21 cm continuum map

No	l ($^{\circ}$)	b ($^{\circ}$)	Type	V_{LSR} (km s^{-1})	Cloud	Ang. size ($'$)	Area (pc^2)	S_{ν} (21 cm) (Jy)	SFR density ($M_{\odot} \text{ yr}^{-1} \text{ kpc}^{-2}$)	Mass (M_{\odot})	Σ_{gas} ($M_{\odot} \text{ pc}^{-2}$)	$\log N_{\text{Ly}\alpha}$ (s^{-1})	# O7V	M_{tot} (M_{\odot})	O7V
1	334.7	0	CH II	-60 to -30	RCW 106	2.6	-	0.48	0.73	-	-	47.68	0	0	
2	334.7	-0.6	CH II	-60 to -30	RCW 106	2.9	-	0.96	1.3	-	-	48	0	0	
3	334.6	-0.1	CH II	-60 to -30	RCW 106	5.5	-	1.8	0.78	-	-	48.31	0	0	
4	334.6	0.4	CH II	-60 to -30	RCW 106	1.6	-	0.12	0.53	-	-	47.21	0	0	
5	334.5	0.8	CH II	-60 to -30	RCW 106	3.7	-	0.29	0.14	-	-	47.76	0	0	
6	334.2	0.1	SNR	-	-	27.7	-	6.4	0.24	-	-	48.88	-	-	
7	333.6	-0.2	GH II	-97 to -78	MCC331-90	31.5	2109.35	-	-	1.7×10^5	80.95	-	-	-	
				-58 to -32	RCW 106		881.48	85	2	2.0×10^5	227.99	50.02	20	500	
8	333.7	-0.4	CH II	-80 to -57	RCW 106	2.1	36.04	0.23	0.61	2.7×10^3	74.15	47.29	0	0	
9	333.3	-0.4	H II	-93 to -77	MCC331-90	16.6	496.31	38	2.2	2.2×10^4	44.45	49.65	-	-	
10	333	-0.4	H II	-76 to -36	RCW 106	19.6	402.26	73	2.6	1.2×10^4	28.77	49.94	17	425	
11	333	-0.7	H II	-76 to -36	RCW 106	12.9	-	4.9	0.57	-	-	48.74	1	25	
12	332.9	0.8	CH II	-80 to -57	RCW 106	5.6	-	6.6	2.1	-	-	48.93	1	25	
13	332.7	-0.6	H II	-60 to -30	RCW 106	16.8	103.62	36	1.6	1.0×10^4	99.17	49.65	8	200	
14	332.5	-0.1	CH II	-106 to -76	MCC331-90	4.3	83.84	1.9	1.1	9.8×10^3	117.17	-	-	-	
				-72 to -32	RCW 106		49.02			3.6×10^3	73.84	48.37	0	0	
15	332.4	0.5	SNR	-	-	14.6	644.09	18	0.96	5.8×10^4	90.73	49.4	-	-	
16	332.4	-0.4	SNR	-	-	9.7	-	20	1.9	-	-	49.41	-	-	
17	332.2	-0.1	CH II	-101 to -77	MCC331-90	1.8	49.64	0.12	0.53	6.4×10^3	129.6	-	-	-	
				-77 to -48	RCW 106		32.21			1.6×10^3	50.44	47.2	0	0	
18f1	333.1	0	CH II	-98 to -82	MCC331-90	3.9	748.75	1.6	1.4	6.0×10^4	80.66	48.26	-	-	
				-73 to -36	RCW 106		469.51			3.8×10^4	81.75	48.26	0	0	
18f2	-	-	CH II	-60 to -30	RCW 106	7.9	-	1.9	0.49	-	-	48.98	1	25	
18f3	-	-	H II	-60 to -30	RCW 106	10.9	-	7.3	1.01	-	-	48.39	0	0	
19	332.1	-0.4	CH II	-61 to -40	RCW 106	7.2	65.68	-	-	2.5×10^3	38.61	-	-	-	
20	331.9	0.2	SNR	-	-	11.1	368.16	3.7	0.56	3.3×10^4	89.6	48.78	-	-	
21	331.6	0	SNR	-	-	13.6	1097.25	41	2.4	1.8×10^5	166.59	49.71	-	-	
22	331.4	-0.3	H II	-107 to -88	MCC331-90	9.7	407.17	7.9	1.5	4.3×10^4	105.16	-	-	-	
				-74 to -36	RCW 106	216.67	-	-	-	3.1×10^4	144.96	48.97	1	25	
23	331.3	0.5	CH II	-61 to -40	RCW 106	8.2	-	2.4	0.59	-	-	48.59	0	0	
24	331.3	0	CH II	-104 to -72	MCC331-90	7.5	154.31	6.3	1.3	2.6×10^4	169.12	-	-	-	
				-72 to -37	RCW 106		96.66			8.2×10^3	84.42	48.91	1	25	
25	331.2	-0.2	CH II	-104 to -79	MCC331-90	4.9	123.88	3.4	1.7	2.3×10^4	183.98	-	-	-	
				-68 to -32	RCW 106	69.47	-	-	-	2.2×10^3	32.31	48.63	0	0	
26	331.1	-0.5	CH II	-68 to -32	RCW 106	3.6	-	0.98	0.69	-	-	48.01	0	0	
26B	-	-	CH II	-68 to -32	RCW 106	3.7	-	1.1	0.84	-	-	48.14	0	0	
26C	-	-	CH II	-68 to -32	RCW 106	5.5	-	3.4	1.3	-	-	48.64	0	0	
27	331.1	-0.2	H II	-101 to -76	MCC331-90	12.3	481.05	9.3	0.95	8.3×10^4	171.78	-	-	-	
				-69 to -33	RCW 106	286.99	-	-	-	1.6×10^4	54.77	49.09	2	50	
28A	330.7	-0.4	H II	-101 to -80	MCC331-90	11.4	528.18	11	1.3	2.9×10^4	55.97	49.15	-	-	
				-69 to -32	RCW 106	332.42	-	-	-	4.1×10^4	122.17	49.15	2	50	
28B	330.7	-0.4	CH II	-69 to -32	RCW 106	3.9	-	1.8	1.4	-	-	47.54	0	0	
28C	330.7	-0.4	CH II	-69 to -32	RCW 106	2.9	-	0.27	0.56	-	-	48.37	0	0	
29	330.3	-0.4	CH II	-80 to -30	RCW 106	2.8	13.68	-	-	1.2×10^3	88.77	48.37	0	0	
30	330.2	1	SNR	-	-	5.9	244	1.3	-	-	-	-	-	-	
31	330.1	-0.1	CH II	-112 to -80	MCC331-90	3.2	45.74	-	-	5.3×10^3	115.8	-	-	-	
				-67 to -33	RCW 106	23.44	0.67	0.86	0.86	1.0×10^3	43.74	47.89	0	0	

A.1. RCW 106: a giant H II Region structure

The H II region complex RCW 106 spans approximately $1^{\circ}5$ in the range $332^{\circ} \leq l \leq 333^{\circ}5$ and so at a distance of 3.6 kpc (Lockman 1979) is of “giant” extent, 94 pc. The structure lies predominately below the Galactic mid-plane. We separated the structure into six components which are large themselves, illustrated in Fig. 8 and described in the brief notes below.

Box 7 (RCW106a). Large in size at nearly 33 pc. It has many known H II regions, star clusters, and SNR G333.6-00.2 which is located at the brightest peak (see Fig. 8a).

Box 9 (RCW106b). An extended structure of ~ 17 pc in length (see Fig. 8b). It has an irregular shape with prominent protrusions. The main intensity peak is crescent shaped.

Box 10 (RCW106c). An irregular H II region with a fairly large main peak and size of almost 9 pc (see Fig. 8c).

Box 11 (RCW106d). An irregular H II region with a fairly large main peak and a tail (see Fig. 8d).

Box 13 (RCW106e). An irregular structure with three main peaks loosely connected and a size of about 17.5 pc (Fig. 8e).

Box 18 (RCW106f). Diffuse H II region with four dominant peaks (Fig. 8f).

A.2. Circularly shaped H II regions

A number of the smaller H II regions in Fig. 1 appear to be fairly “circular” in structure. These are illustrated in Fig. 9 and described below.

Box 1. The compact H II region contains the single IRAS source 16226-4900 at its center.

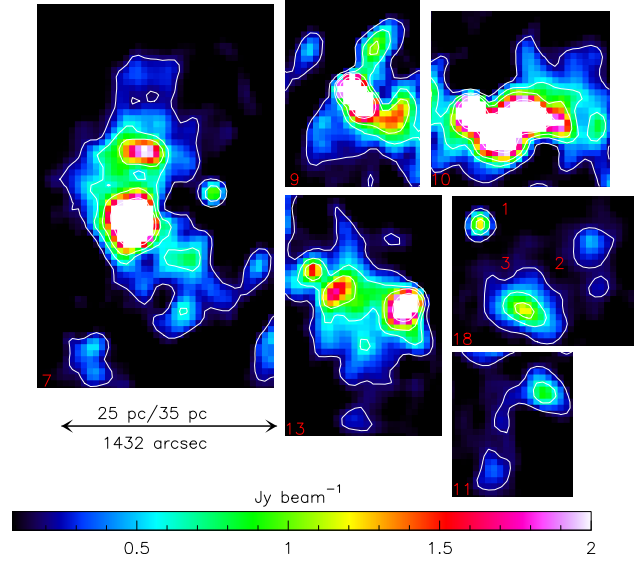


Figure 8. Components of the giant H II structure RCW 106. The distance scales use both near and far kinematic distances.

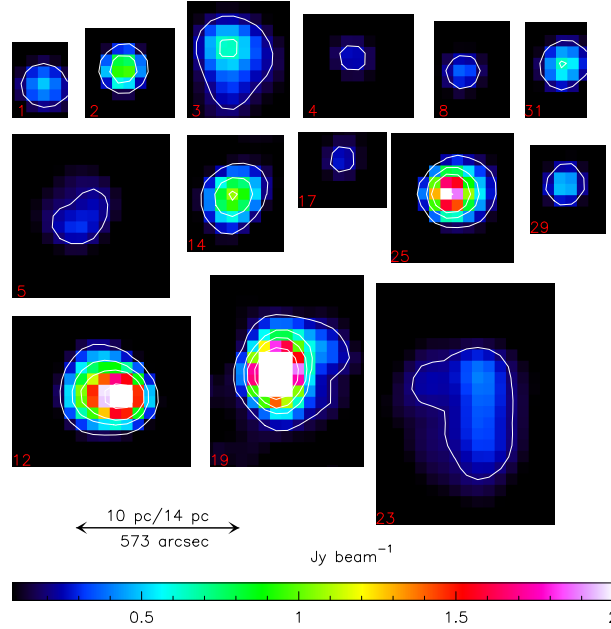


Figure 9. Circularly shaped H II regions. The distance scales use both near and far kinematic distances.

Box 2. An ultracompact H II region coincides with an IR star cluster [DBS 2003] 170.^{xxiii} As discussed by Dutra et al. (2003), the composition is a bit ambiguous but there are a few bright stars. The H II region GAL334.71–00.67 found in this box is 17.4 kpc away as determined by its positive velocity (Russeil et al. 2005).

Box 3. The compact H II region that we detect is roughly 5.8 pc in size and probably coincides with the H II region GAL 334.68–00.11. It has a nearby cluster of IR sources (Robitaille et al. 2008).

Box 4. This compact H II region is roughly 1.6 pc in size, which almost makes it an ultracompact candidate.

Box 5. There is a YSO on the border of the compact H II region. The star cluster [MCM 2005b] 79 (Mercer et al. 2005) is also nearby. This source has a faint protrusion in the lowest contour, not so significant that we describe it as irregular.

Box 8. This compact H II region has a few YSOs nearby.

Box 12. This compact H II region contains the IR star cluster [DBS 2003] 102. It also coincides with the known H II regions GAL 332.98+00.79 and [WHR97] 16112–4943. The latter is classified as UCHII (Walsh et al. 1997).

Box 14. This compact grouping encompasses the known H II regions [KC 97c] G332.5–00.1, GRS 332.54–00.11, and GAL 332.54–00.11 (Kuchar & Clark 1997) and the star clusters [DBS 2003] 160 and 161. This clump is a potential OB cluster as seen from the numerous OB stars within the region. There are also some YSOs and outflow regions within the clump.

^{xxiii} [ref.] # from SIMBAD: <http://simbad.u-strasbg.fr>.

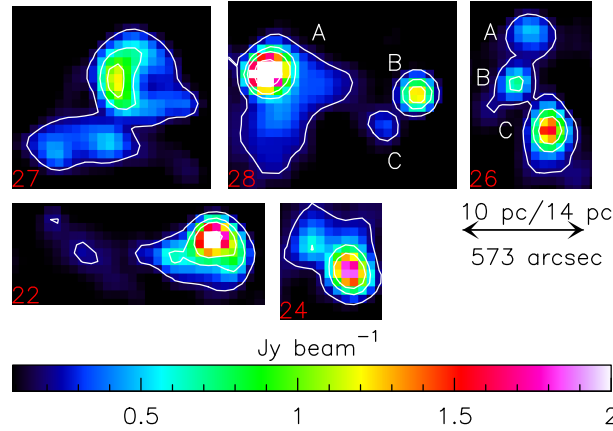


Figure 10. Irregularly shaped H II regions. The distance scales use both near and far kinematic distances.

Box 17. This is the compact H II region *IRAS* 16119-5048 driving an outflow.

Box 19. An H II region hosting a star cluster [MCM 2005b] 74. It has a cometary shape and is significantly brighter with an off-center peak in its circular structure. It is located near the supernova remnant, SNR G332.4-0.4.

Box 23. Most likely the compact H II region GAL 331.36+00.51, the structure is elliptical with a slight protrusion along the longitudinal axis and is 8.6 pc in size.

Box 25. A possible compact H II region. It is ~ 5 pc in size with the known H II regions [KC 97c] G331.3-00.2, GAL 331.28-00.19, and GAL 331.26-00.19 within its peak.

Box 29. A compact H II region, 2.9 pc in size and associated with the IR cluster [DBS 2003] 153. It also hosts the known H II region *IRAS* 16037-5223 and GAL 330.31-00.39.

Box 31. A compact H II region probably powered by GAL 330.04-00.05.

A.3. Irregularly shaped H II regions

The remaining H II regions as seen in Fig. 10 are “irregular” in outline as compared those in Fig. 9. Descriptions of these follow.

Box 22. An extended H II region of ~ 10 pc in size. It has numerous IR star clusters and known H II regions. It displays a comet-like structure with its brightest and largest feature at $331^{\circ}33$. There are two smaller peaks trailing off from the tail. They are diffuse and seemingly attached to the main structure.

Box 24. A compact H II region with the IR star cluster, [DBS 2003] 158. It is elongated and has double peaks. The main peak is off-center in one of the protrusions where the known H II regions are located. It is also near the supernova candidate MSC331.8+0.0 whose structure may be related.

Box 26. The structure is elongated with three main compact peaks that may all be connected. Together they form an elongated structure that is ~ 11 pc in length.

Box 27. Both GAL 331.03-00.15 and PMN J1610-5150 coincides with this H II region. There are numerous OB associations spread around the main intensity peak.

Box 28. This has been subdivided into three regions 28A, 28B, and 28C from largest to smallest with sizes ~ 12 , 4, and 3 pc, respectively. The H II region 28A hosts numerous known H II regions and the IR star cluster [DBS 2003] 155 while 28B appears as a compact H II region with IR star cluster [DBS 2003] 154. 28C is as yet undefined. Individually, 28A has a comet-like shape with two tails while 28B and 28C are circular in nature.

A.4. Supernova remnants and candidates

There are four confirmed and two candidate supernova remnants (SNRs) (Fig. 11). These are seen in projection and are not necessarily associated with the two main star-forming complexes.

Box 6. The SNR Candidate G333.9+00.0 seems very faint with many separated clumps.

Box 15. The SNR G332.4+0.1 has three main peaks that may be part of one shell judging from the contour lines. From OH absorption it is thought to be in the range of 7–11 kpc (Caswell & Haynes 1975).

Box 16. The SNR G332.4-0.4 seems to have a circular shell. A higher intensity portion situated near the bottom is the RCW 103 star cluster. It has a kinematic distance of 3.1 kpc from H I absorption lines (Green 2009).

Box 20. The shell of SNR G332.0+0.2 is a crescent and is thought to be at at least 7 kpc (Caswell & Haynes 1975).

Box 21. The SNR candidate MSC 331.8+0.0 shows a high intensity portion with scattered filaments. Box 30. The SNR G330.2+01.0 has a minimum distance of 4 kpc (McClure-Griffiths et al. 2001).

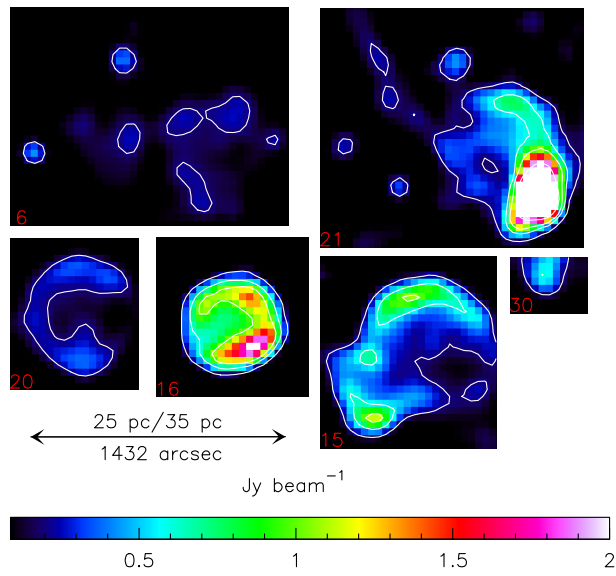


Figure 11. Supernova remnants and candidates. The distance scales use both near and far kinematic distances.